Sustainable Energy Technologies and Assessments 89 (2026) 104997

Contents lists available at ScienceDirect

Sustainable Energy Technologies and Assessments

journal homepage: www.elsevier.com/locate/seta

Original article

Scalable synthesis and electrode engineering of $Li_{1.2}Ni_{0.3}Mn_{0.5}O_2$ and $LiFePO_4$/C cathode materials for 18650 laboratory cells

H.D. Agudelo-Arias [a,b], D.C. Orozco-Gallo [a,*], J.D. Ortiz-Gonzalez [a], F.A. Vásquez-Arroyave [a], J.A. Calderón-Gutiérrez [a,*]

[a] Centro de Investigación, InnovaciónColombia y Desarrollo de Materiales – CIDEMAT, Universidad de Antioquia., Street 70 N# 52 – 21, Medellín, Colombia
[b] Grupo de Investigación en Energías Renovables-GIERMET, Universidad Tecnológica del Chocó, Facultad de Ingeniería, Programa de Telecomunicaciones e Informática, Cra. 22 No 18B-10B, Quibdó, Colombia

ARTICLE INFO

Keywords:
Scalable cathode synthesis
Slurry optimization
Electrode engineering

ABSTRACT

Cathode materials remain a critical challenge for reducing costs and improving durability in lithium-ion batteries. This work presents a scalable method for synthesizing cathode materials and optimizing slurries using a response-surface experimental design to minimize testing while identifying slurry compositions that increase discharge capacity by boosting active-material loading. Two cathode systems: $Li_{1.2}Ni_{0.3}Mn_{0.5}O_2$ on an α-MnOOH template and $LiFePO_4$/C, were synthesized, scaled, and characterized using Raman spectroscopy, XRD, SEM, and electrochemical analysis. Optimized slurries were then evaluated through densification, adhesion (ASTM D3359-2), and mechanical bending/lamination tests to assess their suitability for 18650 cell assembly. Statistical analysis indicated that binder and Super P content negatively affect discharge capacity, whereas electrode thickness and Super P content positively affect it. A dry-film thickness of 30 μm was identified as optimal for calendering, resulting in better malleability and higher capacity. Custom 18650 cells demonstrated that LFP/C offers superior cycling stability and durability, whereas LNMO α-MnOOH provides higher initial capacities. Overall, this integrated workflow offers a scalable pathway from cathode synthesis to electrode fabrication and 18650 lab-cell assembly.

Introduction

Lithium-ion batteries (LIBs) continue to drive the global transition toward affordable and sustainable energy systems. Despite their widespread adoption, significant challenges persist in reducing material costs, improving manufacturing efficiency, and optimizing electrochemical performance. Cathode materials remain a primary target for improvement since they account for up to 45% of total cell cost [1]. Current research efforts have therefore focused on enhancing intercalation-based cathodes. Particularly layered, spinel, and olivine structures for their stability, high energy density, and comparatively low toxicity, with $LiMnNiO_2$ and $LiFePO_4$ (LFP) among the most promising candidates.

Li-rich layered materials ($Li_{1.2}Ni_xCo_yMn_{1-x-y}O_2$) offer high discharge capacities and energy densities [2–4], but their widespread use is limited by low initial coulombic efficiency, voltage fade, and structural instability, issues pronounced at high mass loadings due to restricted Li-ion diffusion and electrolyte penetration [4–7]. In contrast, olivine-type LFP provides excellent structural stability, safety, and long-term cycling performance [8–10], but its intrinsically low electronic conductivity requires strategies such as doping and surface coating to reduce lithium diffusion pathways [10–15]. These characteristics make LFP/C particularly attractive for mobile applications requiring high C-rates and thermal stability despite its modest theoretical capacity (170 mAh g^{-1}) [16,17].

Efforts to reduce costs and increase energy density have intensified interest in scaling electrode fabrication processes for multiple LIB formats, including coin, prismatic, and 18650 cylindrical cells [6,18–20]. Key parameters such as slurry composition, active material loading, electrode thickness, and calendering conditions strongly influence electrode manufacturability and performance [20–24]. Therefore, achieving high-quality thick electrodes requires fine control over slurry rheology, particle dispersion, binder/conductive agent interactions, and mechanical densification to avoid increased tortuosity, cracking, and

* Corresponding authors at: Centro de Investigación, InnovaciónColombia y Desarrollo de Materiales – CIDEMAT, Universidad de Antioquia., Street 70 N# 52 – 21, Medellín, Colombia.
E-mail addresses: dcorozcog@unal.edu.co (D.C. Orozco-Gallo), andres.calderon@udea.edu.co (J.A. Calderón-Gutiérrez).

https://doi.org/10.1016/j.seta.2026.104997
Received 27 February 2026; Received in revised form 20 April 2026; Accepted 21 April 2026
Available online 27 April 2026

poor electrolyte wetting [25–28].

In this work, we present a comprehensive strategy for the scalable synthesis and electrode engineering of Li1.2 N0.3Mn0.5O2 and LiFePO4/C cathode materials for 18650 laboratory cells. Using materials previously optimized in our lab, we employed a Box-Behnken factorial design to identify optimal slurry compositions that maximize discharge capacity and increase active material loading. Additionally, these optimized formulations were incorporated into a scalable electrode engineering process that included controlled-thickness electrode casting, calendering, and mechanical adhesion testing following ASTM D3359-2. Electrodes meeting the necessary adhesion and densification standards were then subjected to C-rate analysis, and a repeated-measures assessment determined the final electrode thickness and calendering pressure needed for robust 18650 cell production. This systematic approach offers a clear pathway from cathode material synthesis to electrode optimization and full assembly of customized 18650 lab-scale cells, establishing a scalable method relevant to next-generation lithium-ion battery development.

Methodology

Fig. 1 summarizes the methodology used in this study. Cathode materials were synthesized under previously established conditions (Section S1) and ground to achieve particle homogeneity. The slurry optimization was carried out by testing 13 compositions in coin cells (200 mg solid content) to maximize active material loading and discharge capacity. The optimal formulation was scaled to a 5 g batch to evaluate casting, adhesion, drying, and calendering parameters required for 18650 cell electrode fabrication. Next, the final electrodes with the selected casting thickness, calendering pressure, and drying conditions were made from a 37 g slurry batch. Finally, the 18650 cells were assembled for performance evaluation.

Cathode materials synthesis

The α-MnOOH and LNMO were synthesized by the hydrothermal method reported in [29], with a modified composition of $Li_{1.2}Ni_{0.3}Mn_{0.5}O_2$ for this study. For the LFP/C, a two-step solvothermal method was employed, as reported by L. Wang et al. [30] (Section S1).

Slurry preparation and optimization

To prepare the slurry, the cathode material (LFP/C or LNMO α-MnOOH) was mixed with PVDF and Super P carbon using N-Methyl-2-pyrrolidone (NMP) as the solvent, at the percentages specified in the experimental design (Table S1). The percentage difference from these gives us the active material content. Then, the mixture was magnetically agitated at 1200 rpm for 24 h at 20 °C. Subsequently, the slurry is applied to an aluminum foil sheet using a doctor blade, with a thickness variation relative to the BDD (Table S1). Then, the electrodes were dried at 80 °C for 12 h, cut, and weighed.

The components ratio slurry ratio was obtained with a Box-Behnken design (BBD) as described in our previous work [31]. The resulting experiments (Table A1), considering the factors presented in Table S1, used discharge capacity, coulombic efficiency, and electrode mass as response variables.

The BDD optimization was performed in coin cells (CR2032) assembled in a MBraun argon-filled glove box with 0.5 ppm water and oxygen. The half-cell contained lithium foil as counter and reference electrode; the electrolyte was prepared by mixing ethylene carbonate (EC)-dimethyl carbonate (DMC) mixture (1:2 ratio, by volume) (Tianci, Guangzhou, China) with 1.2 M $LiPF_6$, and the separator is polypropylene film Celgard 2400 with 16 μm. The cathode potential ranges applied were 2 V to 4.5 V for LFP/C in CC mode and 2 V to 4.8 V for LNMO α-MnOOH in CCCV mode. The C-Rate was performed from 0.2C to 10C for cathode discharge capacity and capacity retention at 25 °C.

Electrode densification and adherence assays

After optimizing the LFP/C and LNMO-α-MnOOH formulations to obtain thicker, and well-adhered electrodes, densification studies were conducted. First, the electrodes' thickness variation from a 5 g batch was dried at 110 °C. Then, electrode flexibility was assessed by bending samples around a 16.32 mm tube, and electrodes with structural integrity were further dried at 80 °C for 12 h. Subsequently, the required pressure was selected to achieve a thickness reduction of 10–40 μm in

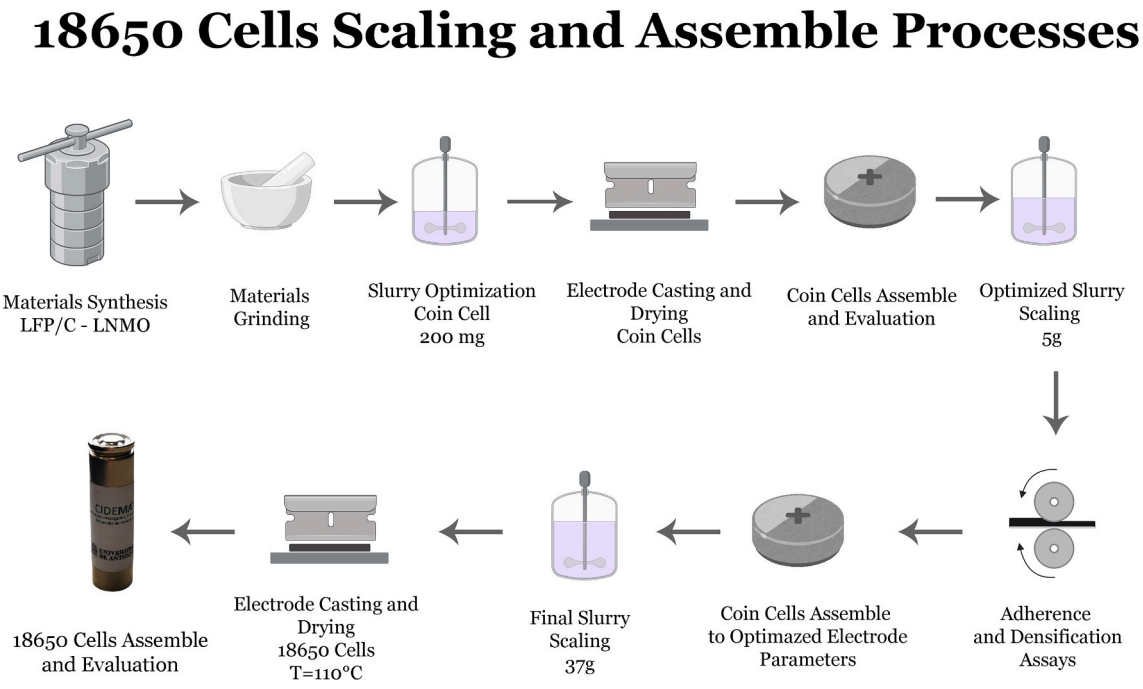

Fig. 1. Methodology to scale and assemble 18650 cells.

the dried and calendered electrodes. Moreover, adhesion was tested with the ASTM D3359-2 Method A. Furthermore, with the selected adhesion and bending conditions, the electrodes were electrochemically evaluated in CR2032 cells. Finally, repeated-measures analysis, supported by ANOVA results (Section S12), enabled the identification of optimal casting and densification conditions for fabricating the final 18650 electrodes.

18650 assembly and evaluation

The final slurry and electrode conditions allowed us to obtain the cathodes, and the anodes were prepared using previously optimized formulations [30] and pressed to a final, dried thickness of 20 μm, which were then rolled onto Celgard 2400 separators for the 18650 cells. Electrode tabs were ultrasonically welded, components were sealed and grooved, and cells were vacuum-dried at 90 °C for 24 h before being filled with 7 mL of 1.0 M $LiPF_6$ in EC/DMC (1:1 v/v) using a controlled fill–vacuum sequence, after which the lids were sealed.

Assembled cells were balanced at a 1:1 anode-to-cathode capacity ratio and rested for 24 h before three formation cycles at 40–80 mA in voltage windows of 2.5–4.2 V (LFP/C) or 2.5–4.5 V (LNMO α-MnOOH) at 25 °C until reaching 99% coulombic efficiency. Cells meeting this threshold were cycled at the same current for stability evaluation until coulombic efficiency declined. After testing, cells were stored fully charged, stabilizing at 3.9 V for layered-oxide cathodes and 3.3 V for olivine-type cathodes.

Samples characterization

The physicochemical characterization of the samples using SEM, Raman, XRD, rheology, and BET is described in Section S2.

Results and discussion

LNMO α-MnOOH and LFP/C materials synthesis

Fig. 2 illustrates XRD and Raman spectra for the scale synthesis of LNMO α-MnOOH. XRD and Raman analyses confirmed the structure and variations of scaled LFP/C and LNMO α-MnOOH materials. Fig. 2b shows the LFP/C Raman spectrum, with overlapping signals from the carbon coating and olivine. Vibrations at 219, 289, 401, and 610 cm^{-1} correspond to A1g, Eg, Eg (O-Fe-O bending of α-Fe_2O_3), and Eg (Fe-O stretching of α-Fe_2O_3). Fe_2O_3, from Fe^{2+} oxidation during synthesis, appears as a sharp band at 946 cm^{-1} (υ1 mode). The 1340 cm^{-1} D-band and 1580 cm^{-1} G-band indicate olivine-related peaks. Despite Fe_2O_3 impurities potentially reducing active sites for lithium, low diffraction peak intensity limits reliable analysis; only a qualitative assessment is made.

Fig. 2a exhibits the XRD pattern of the orthorhombic structure and spatial group *Pnma* (ICSD 98–009-9860) for the $LiFePO_4$ [32] where the higher intensity peak (311) was associated with LFP morphology with bc orientation [33]. Regarding the LNMO α-MnOOH sample, the diffraction pattern in Fig. 2c shows two crystalline phases: the Li-rich layers with a rhombohedral structure and space group $R\bar{3}m$ (ICSD 98–005-5369) and a monoclinic structure with space group C2/m (ICSD 98–002-1022). The corresponding weak peaks in the 2Θ range 20–25° with the plane (110) correspond to the monoclinic phase [34]. Moreover, the LNMO α-MnOOH Raman spectrum (Fig. 2d) exhibits a shoulder band on the left side of the E_g vibration mode related to the monoclinic phase at 428.5 cm^{-1}. Table S2 reports the Rietveld refinement parameters for the XRD patterns of both samples. LNMO α-MnOOH, refined in the rhombohedral $R\bar{3}m$ structure (hexagonal setting), has lattice parameters a = b = 2.863(5) Å, c = 14.21(7) Å, and unit-cell volume 100.88(61) $Å^3$. LFP, in the orthorhombic Pnma structure, has a = 10.28(1) Å, b = 5.96(1) Å, c = 4.677(5) Å, with a volume of 286.86(64) $Å^3$. These align with literature reports for orthorhombic $LiFePO_4$ and Li-rich layered cathodes like $Li_{1.2}Ni_{0.3}Mn_{0.5}O_2$, which often have a rhombohedral $R\bar{3}m$ framework

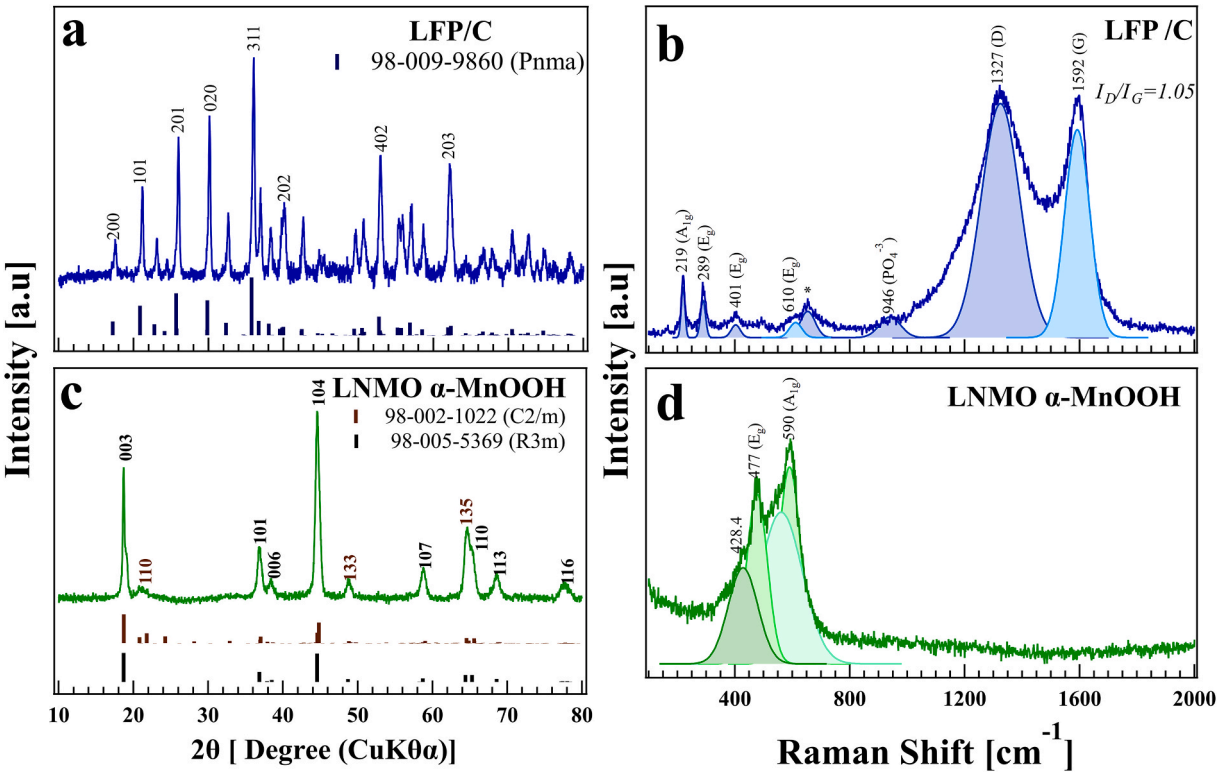

Fig. 2. XRD and Raman and spectra of the synthesized scaled materials. LFP a) and b), LNMO α-MnOOH c) and d).

with possible C2/m ordering.

Furthermore, the LNMO α-MnOOH active material displays two broad bands, indicating variations in the local oxygen environment [35,36]. The broad bands located at 477 cm^{-1} and 590 cm^{-1} correspond to the Eg vibration mode along the O-layers and the A_{1g} symmetry mode along the c-axis, respectively [35,36]. The broad bands confirmed that the rhombohedral phase is well-formed after scaling.

LNMO α-MnOOH and LFP/C electrodes optimization

The ANOVA results (Tables S3–S8) show that binder content significantly improves coulombic efficiency for LNMO α-MnOOH cathodes (Table S3), explaining 82.26% of the variation (R^2), and the binder-Super P interaction has a negative effect. Moreover, for LFP cathodes (Table S8), mass deviation displayed a strong correlation with thickness (R^2 = 84.7%), whereas coulombic efficiency showed no meaningful factor dependence (R^2 = 74.6%).

Discharge capacity showed the greatest sensitivity to formulation parameters, as indicated by the Pareto analyses for both materials (Fig. 3b, e). For LFP/C, electrode thickness and Super P content positively influenced capacity, whereas the binder-Super P interaction was detrimental (Fig. 3b), consistent with the factor effect plot (Fig. 3c). ANOVA results (Table S3) identified significant contributors ($p < 0.05$), including thickness (C), binder (A_2, B_2), the binder–Super P interaction

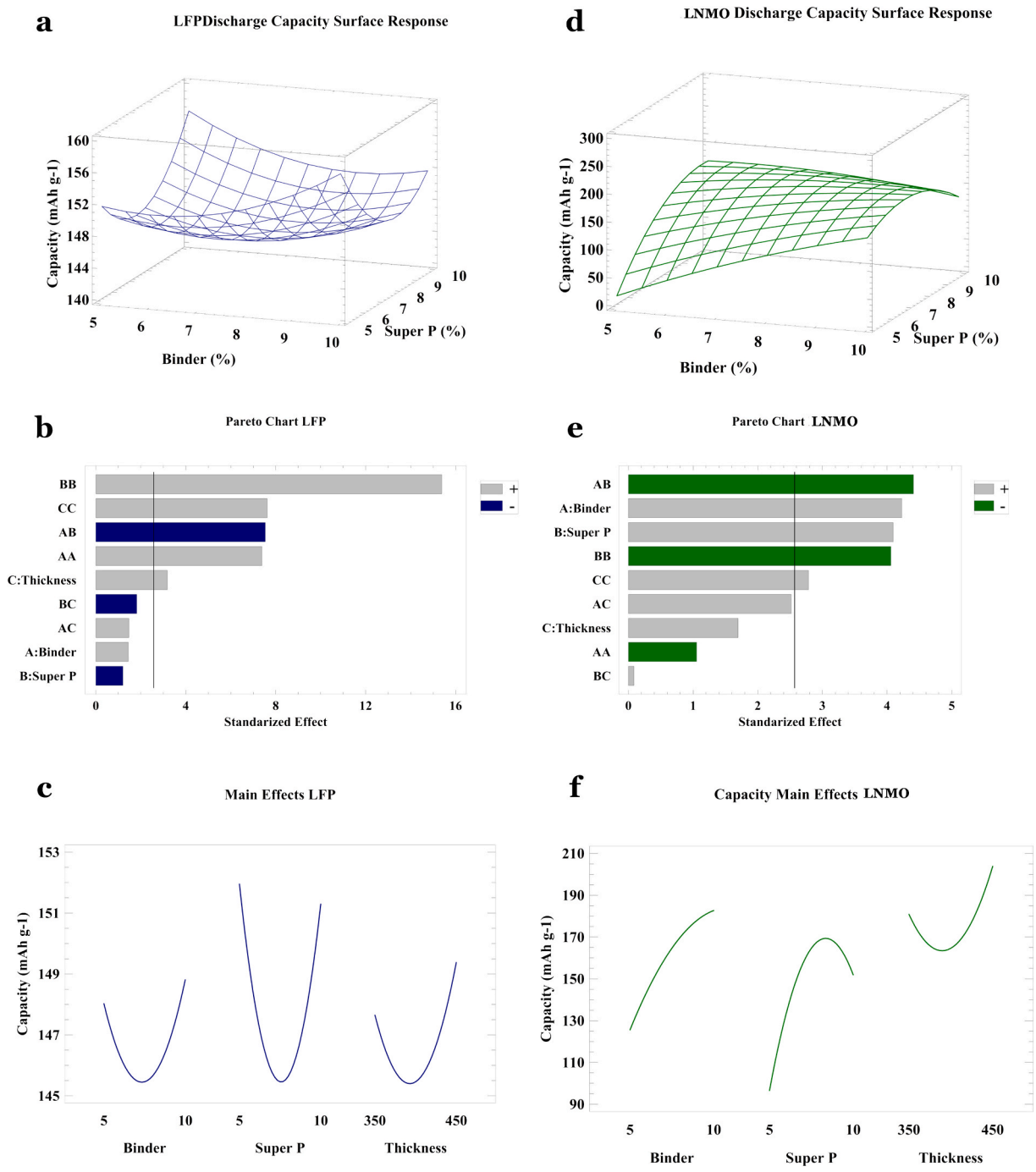

Fig. 3. Statistical analysis of discharge capacity for the LFP/C and LNMO α-MnOOH materials. LFP: a) Optimization curve, b) Pareto diagram, c) Factor effects, LNMO α-MnOOH: d) Optimization curve, e) Pareto diagram, and f) Factor effects.

(AB), and thickness (C^2). The response surface (Fig. 2a, Equation (S2)) showed strong model agreement (R^2 = 98.73%), despite the initial factor range not being optimal. Table S9 summarizes the optimal parameters for maximizing LFP/C discharge capacity.

For LNMO α-MnOOH, the ANOVA trends for discharge capacity are like those of LFP/C. Carbon black content, binder percentage, and the thickness term positively affect capacity (Fig. 3e), and the binder-carbon black interaction and binder exert negative influences, as indicated in the effect plot (Fig. 3f). Significant factors identified in Table S2 ($p < 0.05$) include A (Binder), B (Super P), AB (Binder/Super P), B^2 (Super P), and C^2 (Thickness). The response surface (Fig. 3d, Equation (S2)) demonstrates good model fit (R^2 = 94.77%), confirming that the selected factor ranges were appropriate. Table S9 summarizes the optimal parameters to maximize LNMO α-MnOOH discharge capacity.

Electrodes characterization

The BBD optimization results, together with slurry rheology and viscosity–shear-rate behavior (Figure S1), clarify how slurry composition influences electrochemical performance during scaling. Morphology and particle size from SEM analyses (Fig. 4) were compared with the best and worst electrochemical outcomes. The LFP/C sample exhibits the expected olivine structure with 1D Li^+ diffusion channels along the b-axis [37,38] and displays particles 20–30 nm wide, ~100 nm long, and averaging 112.9 nm in size (Figure S2, Table 1). The combination of nanoscale dimensions, 1D transport features, and a carbon coating enhances Li-ion mobility and reduces polarization [39,40].

The positive influence of carbon black on discharge capacity arises from its interaction with PVDF, in which polymer chains adsorb onto particle surfaces while their free segments interact with the solvent, promoting bridging flocculation and generating stable slurries, consistent with Ouyang et al. [28]. Although LFP/C samples display only small capacity differences (Fig. 5, S3), the more stable slurry produces cathodes with a more uniform and broader pore-size distribution (Fig. 4a, c; Table 1) compared to the poorer-performing counterpart (Fig. 4g, i; Table 1). These structural features reduce polarization, enhance electrolyte–electrode contact, and improve rate capability, as confirmed by C-rate results (Fig. 5, S3).

The LNMO α-MnOOH cathodes showed substantial capacity variation during optimization (Fig. 5, S4), highlighting the strong dependence of their electrochemical response on morphology and slurry interactions (Fig. 4g, j, S4). Layered materials typically exhibit 2D ion-transport pathways and high surface-area-to-volume ratios that enhance structural stability under cycling, though they often suffer from restacking and limited 2D charge transport [39]. Incorporating 3D nanorod supports, as in the LNMO α–MnOOH structure (Figure S5), improves charge transport within nanoscale primary particles while enabling higher density and volumetric energy in the micron-scale secondary aggregates due to shorter Li–diffusion paths.

Morphologically, the best-performing LNMO α-MnOOH electrode (Fig. 4g) exhibited a pore-radius distribution of 1–10 μm and global porosity of 0.22 (Fig. 4g, h, j), associated with its higher binder content (10%). In comparison, the poorest performing (Fig. 4j, k, l) showed a broader 1–12 μm pore distribution and higher global porosity (0.35), consistent with its lower binder content (5%). These observations support the BDD findings and confirm the positive effect of binder content on discharge capacity. Therefore, reduced porosity and improved secondary-particle organization in the compacted electrodes facilitate faster Li-ion transport and enhance lithiation/delithiation kinetics within the primary nanoparticles.

The 3D hierarchical morphology of LNMO α–MnOOH enhances volumetric energy density by enabling micron-scale secondary particle growth, while fast kinetics in nanoscale primary particles contribute to higher capacities (Fig. 5). In contrast, LFP/C naturally forms compact, low–porosity structures (Figure S7), resulting in minimal capacity variation with slurry modifications. For LNMO α–MnOOH, however, slurry adjustments markedly influence electrode compactness and thereby Li^+ transport, as its anisotropic 3D diffusion channels benefit from reduced porosity and improved structural packing, significantly improving C–rate performance.

Fig. 5 compares the performance of C-rate, with LNMO α-MnOOH

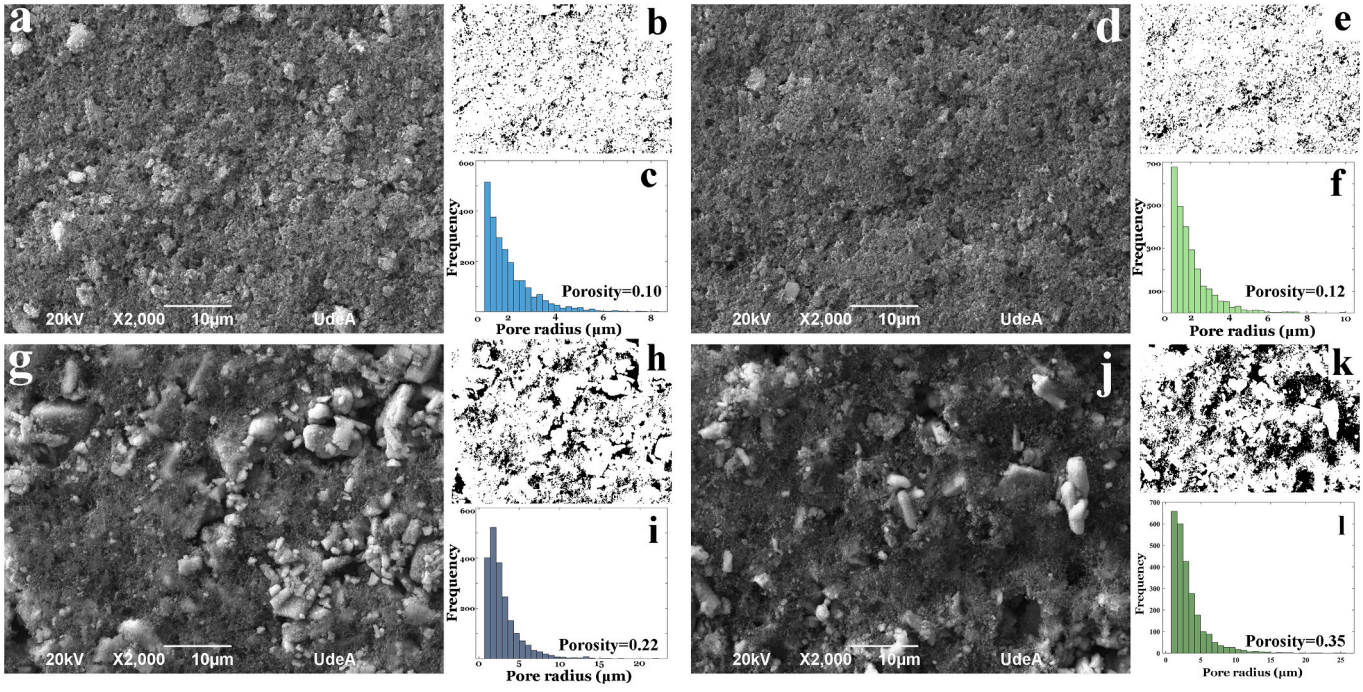

Fig. 4. Morphology for the best and worst cathode materials. LFP/C E5-400 μm: a) SEM, b) Binary Segmentation, c) Pore size distribution. LFP/C E7-400 μm: d) SEM, e) Binary Segmentation, f) Pore size distribution. LNMO α-MnOOH E8-450 μm: g) SEM, h) Binary Segmentation, i) Pore size distribution. LNMO α-MnOOH E8-450 μm: j) SEM, k) Binary Segmentation, and l) Pore size distribution.

Table 1
Summarized results of the best-performing cathodes.

Run	Discharge Capacity (mAh g^{-1})	Coulombic Efficiency (%)	Porosity	Viscosity (Pa s)	Average particle size (nm)	Areal Mass Loading (mg cm^{-2})	Apparent Electrode Density (mg cm^{-3})
LFP/C E5 400 μm10%PVDF – 5%SuperP	158.19	99.1	0.0989	0.1086	112.9	4.46	31.87
LNMO α-MnOOH E8 450 μm10%PVDF –7.5%SuperP	263.67	99.01	0.2207	0.1072	112.9	3.67	59.5

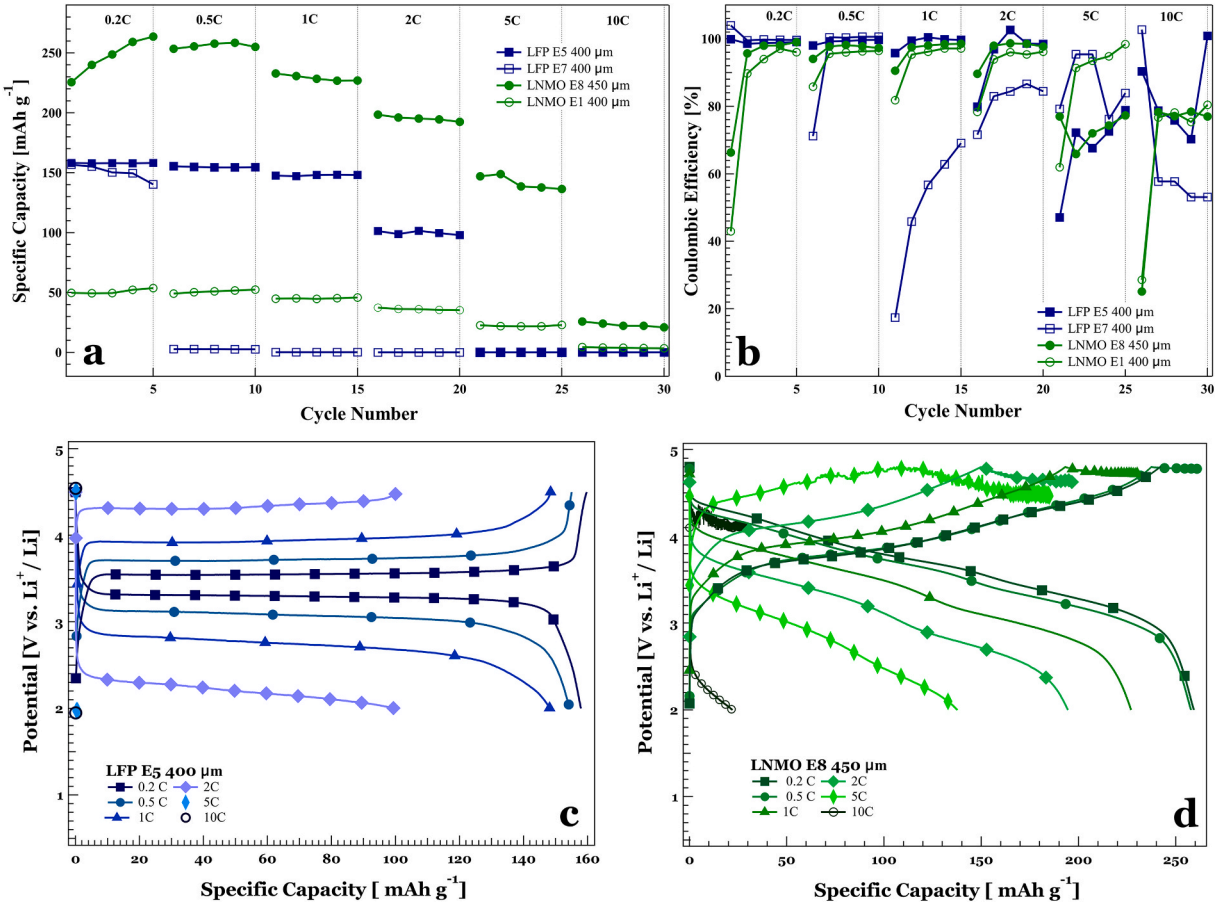

Fig. 5. Electrochemical results for the best and worst-performing materials. a) Discharge capacity, b) Coulombic efficiency. Charge/discharges curves c) LFP, and d) LNMO α-MnOOH.

outperforming LFP/C, showing discharge capacities ranging from 50.20 mAh g^{-1} (worst case) to 263.67 mAh g^{-1} (best case) at 0.2 C and Coulombic efficiencies of 99.01% (Fig. 5a, b; Table 1). Additionally, enhanced lithiation and delithiation kinetics result from reduced porosity and increased electrode surface area. Compactness lowers tortuosity and promotes Li-ion mobility. These effects stem from the combined influence of binder content and calendering on particle adhesion and transport pathways within both 1D and 2D structural frameworks.

The mobility effects observed in the electrodes align with the BET results for both the synthesized materials and the BDD-optimized powders (Table S18). LFP/C shows a higher surface area, larger pore size, and greater pore volume, with macropores helping electrolyte penetration and reducing the negative impacts of added binder and conductive agents. Micropores mostly remain accessible due to polymer distribution through bridging flocculation [28], as seen in LFP-E5 (400 μm, 10% PVDF, 5% Super P). However, excess carbon black causes particle agglomeration that blocks electrolyte pathways, as in LFP-E7 (400 μm, 5% PVDF, 7.5% Super P), which ultimately lowers electrochemical performance. This is especially harmful for LFP/C, where 1D Li^+ transport is sensitive to blocked electrolyte contact, increased interparticle resistance, and hydrophobic barriers that prevent electrolyte wetting.

In contrast, the LNMO α-MnOOH exhibited a lower surface area and a smaller specific pore volume. Consequently, adding a small amount of binder and Super-P mainly increases mesoporosity by creating interparticular spaces [41], as observed in LNMO α-MnOOH (E1 400 μm, 5% PVDF, 5% Super P). However, since lithium-ion transport occurs in 2D through the interlaminar planes, reducing the transport distance improves lithium insertion into the structure, while decreasing interparticle resistance increases the number of active sites involved in the reaction (LNMO α-MnOOH E8 450 μm, 10% PVDF, 7.5% Super P) [39].

The final electrode composition strongly affects the LNMO electrochemical performance LNMO, which has a smaller surface area and pore volume than LFP (Table S18; Figures S12–S13). At low binder levels (LNMO-E1), the surface area stays like the synthesized powder, but increased microporosity occurs due to conductive-agent-induced agglomeration. Insufficient binder weakens bridging flocculation [42],

leading to poorer particle dispersion, longer Li-ion diffusion paths, and reduced electrochemical performance (Fig. 5a). Conversely, higher binder amounts (LNMO-E8) decrease microporosity and strengthen bridging flocculation, improving particle cohesion and contact between active-material domains [41]. This increases Li-ion mobility, resulting in significantly better discharge performance (Fig. 5a). Overall, the combined effects of slurry composition, calendering, and electrode morphology determine Li-ion transport efficiency and, consequently, the final discharge capacity. Rate-dependent charge–discharge curves reveal distinct reaction mechanisms for LFP and LNMO cathodes (Fig. 5c and d). LFP has a flat plateau at ~3.4 V vs. Li^+/Li, indicating a two-phase Fe^{2+}/Fe^{3+} reaction, with increased polarization at higher currents, suggesting phase-boundary and transport limitations[43]. LNMO shows sloped high-voltage plateaus around 4.7 V vs. Li^+/Li, linked to Ni^{2+}/Ni^{4+} redox, and around 4 V for Mn^{3+}, with voltage hysteresis and capacity loss at high rates indicating interfacial and surface kinetic barriers [44].

Densification analysis

Based on the ratios of binder, conductive material, and active material (Table S9), a densification process was performed by preparing and applying slurries with different wet-paint and dried thicknesses. As a result, the samples were named according to the type of cathodic material (LNMO α-MnOOH or LFP/C), the wet paint thickness (t), and the lamination thickness reduction (L), as shown in Tables S10 and S11. Table S11 shows that the maximum wet-coating thickness achievable for LNMO α-MnOOH without affecting electrode flexibility, adhesion, or bending performance is 400 μm. After lamination, adhesion to the aluminum current collector improved, but thickness reductions exceeding 40 μm adversely affected adhesion and capacity. For LFP/C (Table S10), the slurry had higher viscosity, resulting in thicker, heavier coatings than those used for small-scale electrodes; therefore, a lower wet thickness was necessary during densification. The carbon coating also caused slurry lumps, reducing coating uniformity and requiring lamination, although it did not significantly affect adhesion or bending behavior.

Repeated-measures analysis was used to evaluate the effects of casting thickness, calendering pressure, SEI stabilization cycles, and C-rate performance in 18650 cells (Figure S11; Tables S14–S17). LFP/C exhibited minimal capacity variation with changes in thickness or calendering (Figure S10a), although C-rate capability notably decreased at currents above 0.5 C after calendering (Figure S11b). Conversely, LNMO electrodes proved highly sensitive to calendering: increased pressure led to reduced discharge capacity and diminished C-rate capability above 0.2 C (Figure S11c).

These results indicate that the optimal processing conditions are a 300 μm coating thickness with a 30 μm calendering reduction for LFP/C, and a 250 μm thickness with a 30 μm reduction for LNMO α-MnOOH. Additionally, 3–5 formation cycles at 0.2 C are required in 18650-type cells to ensure stable SEI formation and reliable discharge performance. Increasing electrode thickness does not significantly affect specific capacity at 0.2–0.5 C. However, lamination compaction decreases C-rate capability, especially for thicker electrodes (Fig. 6a, b). Furthermore, a thicker electrode needs shorter length to maintain the correct roll diameter for the 18650-cell format.

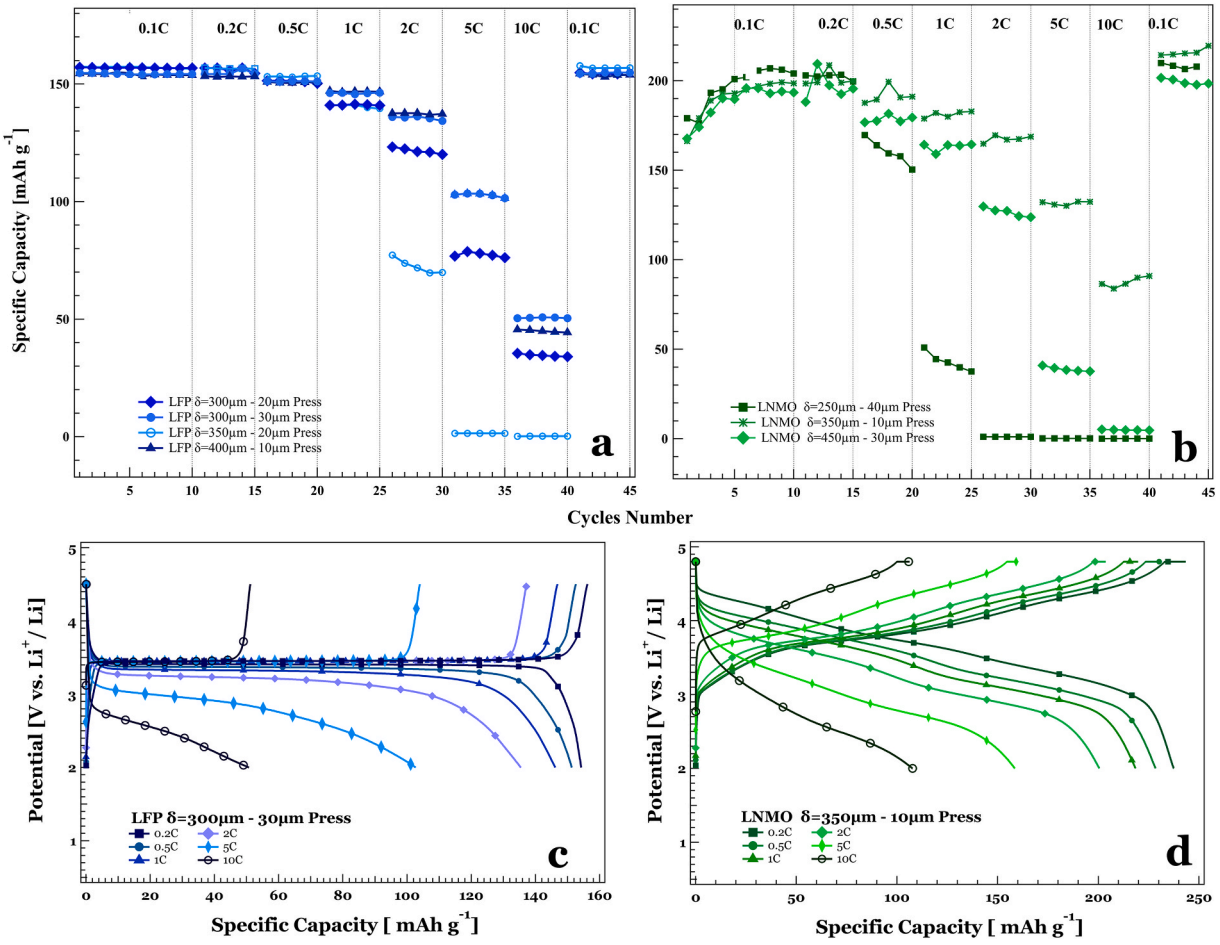

Fig. 6. Electrochemical results for some selected electrodes in the densification analysis. a) LNMO α-MnOOH, b) LFP/C, c) charge/discharges curves for LFP, and d) charge/discharges curves for LNMO α-MnOOH.

Morphological analysis revealed clear structural differences among optimized, scaled, and densified electrodes for both LFP/C and LNMO α-MnOOH materials. Optimized LFP/C electrodes showed a compact, uniform structure (Figs. S9a, S7a) with low porosity (0.1807; Fig. S9b; Table S12), which correlates with their improved electrochemical performance. Scaling up the LFP/C synthesis caused significant particle clumping (Fig. 7c, S7c), making slurry preparation more challenging and resulting in less uniform coated and pressed electrodes, with increased porosity of 0.3299 (Fig. S9d; Table S12). Additional lamination expanded pore size because internal structural rearrangements created heterogeneous regions, thereby reducing capacity in densified electrodes.

For LNMO α-MnOOH, the optimized electrode also exhibited a dense and uniform morphology (Fig. 7e, S8a) with a porosity of 0.1693 (Fig. S9f; Table S12), which accounts for the performance gains after slurry optimization. Unlike LFP/C, the scale-up process maintained particle characteristics, enabling slurry preparation like the optimized formulation (Figs. S9g, S8c). However, porosity increased to 0.3019 in the scaled-up electrode (Fig. S9h; Table S12), likely due to detachment effects during high-temperature drying. Additionally, pore radius increased in the scaled, densified, and pressed electrodes (Fig. S9h; Table S12), because lamination forces caused particle movement and rearrangement, shifting 3D agglomerates of LNMO α-MnOOH and broadening the pore distribution.

Cylindrical lab-cell results

The electrochemical performance of LFP/C and LNMO α-MnOOH 18650 cells was assessed within voltage windows of 2.0–4.0 V and 2.0–4.5 V, respectively, with key results summarized in Table S13. Cycling at 0.2C (40 mA for LFP/C and 80 mA for LNMO α-MnOOH), as shown in Fig. 7, enabled capacity evaluation while maintaining cell integrity. Coulombic efficiencies stabilized at 96–97% after SEI formation, which occurred by cycle 3 for LNMO α-MnOOH and cycle 7 for LFP/C. LFP/C demonstrated superior cycling stability, retaining 75.9% of its capacity after 100 cycles, whereas LNMO α-MnOOH sustained less than 60% retention after 45 cycles. Initial specific capacities and coulombic efficiencies were 0.129 Ah and 54.8% for LFP/C, and 0.23 Ah and 54.02% for LNMO α-MnOOH. The LNMO α-MnOOH cell exhibited a gradual capacity increase to 0.33 Ah over the first 24 cycles before stabilizing until failure at cycle 45. In comparison, the LFP/C cell reached 0.134 Ah by cycle 2 and remained stable through 100 cycles. Both full cells were cycled at 100% depth of discharge using discharge and charge cutoffs of 2.0 V and 4.5 V (LNMO α-MnOOH) or 4.0 V (LFP/C), ensuring complete Li^+ utilization without inducing phase transitions.

The charge–discharge voltage profiles of the LFP/C and LNMO α-MnOOH 18650 cells (Fig. 7b-c) show the characteristic electrochemical features of each system within their respective voltage ranges. For LNMO α-MnOOH, two distinct regions appear during charging at approximately 3.8 V and 4.2 V, corresponding to sequential $Ni2^+/Ni3^+/Ni4^+$ oxidation in $LiMO_2$ (M = Mn, Ni). An initial plateau at 2.9–3.3 V results from electrolyte decomposition and SEI formation on the anode. During discharge, plateaus related to $Ni4^+/Ni3^+$ and $Ni3^+/Ni2^+$ reduction appear near 4.3 V, and a smaller region at around 3.2 V reflects $Mn4^+/Mn3^+$ reduction. The LFP/C cell shows the typical delithiation/lithiation plateau of $Fe2^+/Fe3^+$ redox between approximately 3.2–3.6 V, with an SEI-related feature at 2.8 V during the first charge. Although LNMO α-MnOOH provides a larger initial discharge capacity, indicating a greater ability to release additional Li^+, the LFP/C cell exhibits better long-term stability, maintaining performance over 100 cycles. Variations in the potential profiles of both systems are influenced by the anode's graphite plateaus [45].

The reduced cycling stability of the LNMO α-MnOOH system can be attributed to the behavior of its active phases during high-voltage operation. This material contains both a rhombohedral $LiMO_2$ phase and a monoclinic Li_2MnO_3-like component [29,46], the latter of which becomes activated near ~4.4 V, releasing oxygen and lithium and causing the characteristic capacity increase after the first discharge [47]. However, this activation also leads to structural degradation, poorer capacity retention, and overall inferior electrochemical performance. Since cycling above 4.5 V in 18650 full cells raises safety concerns about overpressure from SEI formation, only the monoclinic phase is effectively activated at the applied cutoff voltage [47], preventing full lithium extraction during early cycles. Additionally, layered materials derived from sacrificial α-MnOOH templates often exhibit slow electrolyte wettability, further hindering Li^+ extraction and contributing to performance losses [29].

The performance decline observed during cycling, especially in the

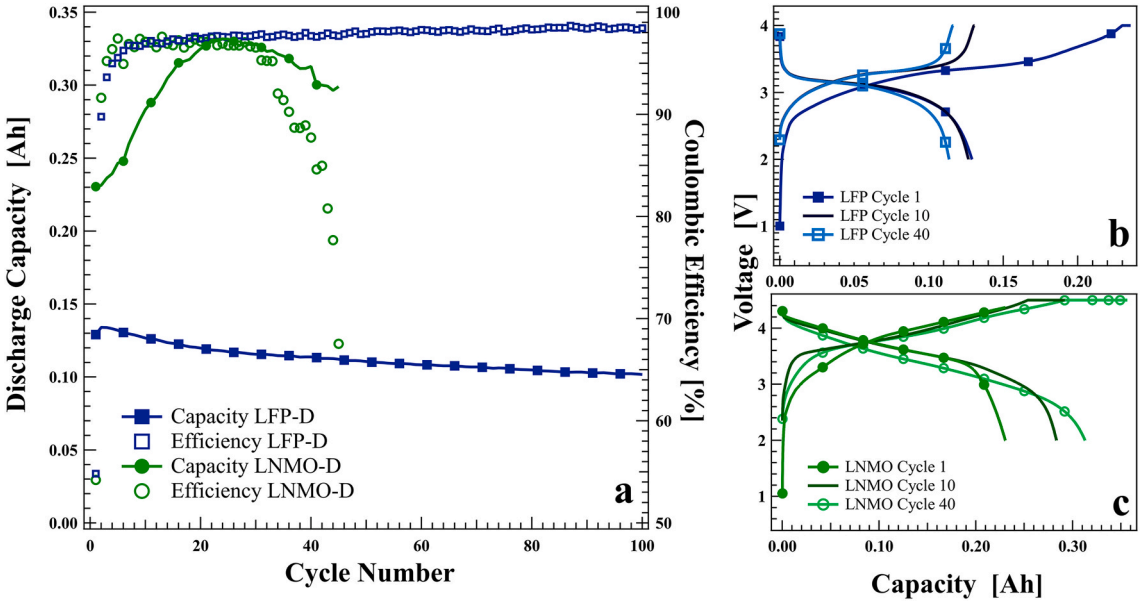

Fig. 7. A) cycling performance in the voltage window from 2.0 to 4.5 V in CCCV mode for the 18650 cells fabricated with LNMO α-MnOOH and 2.0–4.0 V in CCCV mode for LFP/C active cathode materials. b) Charge–discharge voltage profiles of the LFP/C cells between 2.0 and 4.0 V at 20 °C. c) Charge–discharge profiles of the LNMO α-MnOOH cells between 2.0 and 4.5 V at 20 °C.

LNMO α-MnOOH material, is mainly linked to electrolyte interactions that worsen structural instability [48,49]. In these dual-phase systems, lithium transport causes lattice stress along the c-direction, leading to transition-metal migration and resulting in capacity and voltage loss. Several strategies have been suggested to enhance cycling stability, including doping, surface coating, and the use of CEI-stabilizing electrolytes. Doping aims to prevent lattice oxygen loss by strengthening TM–O covalency or improving bond stability by adding 4d or 5d transition-metal ions such as Cu, W, Fe, V, Nb, or Mg [49]. Electrolyte-based methods employ additives like LiDFOB and $LiBF_4$, [50] which reduce side reactions at high depth of discharge and have shown capacity retention improvements of up to 83% after 100 cycles [48] Additionally, modifying the cathode surface with coatings or encapsulation further stabilizes the CEI.

Additionally, electrolyte decomposition occurs in the graphite anode full cell using the common electrolyte (1 M LiPF6 in a mixture of EC/DEC/EMC at a weight ratio of 3:5:2). As a result, lithium reacts, affecting retention capacity and coulombic efficiency. Finally, surface coatings with conductive carbonaceous materials or less reactive cathode materials, such as lithium olivine, have been suggested to protect the active material from dissolution or electrolyte attack. In contrast, the LFP/C cell with orthorhombic olivine is known for its stable structure. Due to its 1D features and particle size, it exhibits low polarization because of increased contact between the electrode's active sites and the electrolyte; therefore, once the maximum coulombic efficiency is reached, the rate capability remains stable even after 100 cycles.

Conclusions

Upscaling cobalt-free LNMO α-MnOOH and $LiFePO_4$/C cathodes shows promise for cheaper and more adaptable future Li-ion batteries. Process optimization revealed that binder-carbon interactions are key in affecting electrode performance. Changes in slurry composition impacted surface area and specific volume, which in turn modified Li-ion transport pathways and ultimately influenced electrochemical behavior. These results emphasize the importance of engineering binder/carbon interfaces to enhance not only capacity and rate capability but also electrode uniformity, mechanical strength, and adhesion to the current collector.

Densified electrodes produced with this optimized method showed excellent compactness, allowing a 30 μm reduction in thickness while maintaining strong adhesion, good mechanical flexibility, and satisfactory electrochemical performance. These are essential features for efficient roll-to-roll manufacturing of 18650 cylindrical cells. Among the assembled cells, the LNMO α-MnOOH 18650 device achieved a higher initial capacity than its LFP/C counterpart. However, both systems exhibited low first-cycle coulombic efficiencies (<54%) due to lithium consumption during solid/electrolyte interphase (SEI) formation. Although LNMO α-MnOOH cells offered better initial discharge capacities, the LFP/C cells demonstrated significantly improved cycling stability at 100% depth of discharge, maintaining over 77% capacity after 100 cycles. This strong retention corroborates the durability potential of the scaled LFP/C materials.

Overall, the results confirm that both the Li-rich layered LNMO α-MnOOH and olivine-type LFP/C materials are promising candidates for cost-effective, in-house 18650 cell manufacturing. Future research should focus on improving the cycling stability of LNMO α-MnOOH through targeted modifications such as elemental doping, surface coatings, or CEI-enhancing electrolyte formulations. Additionally, the excellent rate capability achieved with LFP/C verifies the effectiveness of our integrated methodology, from slurry formulation to calendering, in producing high-quality cylindrical cells. Focusing on slurry stability, component interactions, and densification will be key to further increasing capacity and advancing the development of next-generation, in-house 18650Li-ion cells.

Author Contributions

Hector Agudelo: Material characterization experiments, electrode preparation, and electrochemical measurements. Diana Orozco: Material and slurry characterization and optimization, electrode preparation and electrochemical measurements, methodology, formal analysis, writing, reviewing, and editing. Jessica Ortiz: densification and adherence studies, sample fabrication, densification and batteries 18650 analysis and writing. Ferley. A. Vásquez: densification and adherence studies, sample fabrication and evaluation, formal analysis, writing, and reviewing. Jorge A. Calderón-Gutiérrez: Conceptualization, writing, reviewing, and editing. Project management and supervision

CRediT authorship contribution statement

H.D. Agudelo-Arias: Methodology, Formal analysis, Data curation, Conceptualization. **D.C. Orozco-Gallo:** Writing – original draft, Validation, Project administration, Investigation, Formal analysis, Conceptualization. **J.D. Ortiz-Gonzalez:** Methodology, Investigation, Formal analysis. **F.A. Vásquez-Arroyave:** Writing – review & editing, Validation, Methodology, Investigation, Formal analysis, Conceptualization. **J. A. Calderón-Gutiérrez:** Conceptualization, Writing – review & editing, Project administration, Supervision.

Declaration of competing interest

The authors declare the following financial interests/personal relationships which may be considered as potential competing interests: Jorge Andres Calderon Gutierrez reports financial support was provided by Colombia Ministry of Science Technology and Innovation. Diana Constanza Orozco Gallo reports financial support was provided by Colombia Ministry of Science Technology and Innovation. Hector Agudelo reports financial support was provided by Colombia Ministry of Science Technology and Innovation. Jessica Ortiz reports financial support was provided by Colombia Ministry of Science Technology and Innovation. Ferley Vasquez reports financial support was provided by Colombia Ministry of Science Technology and Innovation. If there are other authors, they declare that they have no known competing financial interests or personal relationships that could have appeared to influence the work reported in this paper.

Acknowledgments

The authors thank “Ministerio de Ciencia Tecnología e Innovacion - Minciencias” for the financial support provided by 890-2020 call for the strengthening of CTeI in public higher education institutions under the project: “*Desarrollo de ensambles de baterías a partir de nuevos materiales y baterías reutilizadas para almacenamiento de un sistema solar fotovoltaico”* Contract No. 2023-0685 Project 82459.

H. Agudelo thanks the Faculty of Engineering of the Technological University of Choco for making the participation in the project and developing the doctoral formation course at the University of Antioquia possible. H. Agudelo also thanks the Colombian Ministry of Science, Technology, and Innovation – “Minciencias” for the PhD scholarship 1 of 2020- Bicentennial Excellence 1. Likewise, thanks to the project “Development of Scientific Capacities for the Investigation of Infrastructure Deterioration Processes in Renewable Energy Systems in the Department of Chocó” BPIN: 2020000100330, executed by the Technological University of Chocó and the Center for Research in Renewable Energies and Climatology for technical support and advising.

Appendix A

Table A1
Box-Behnken experimental conditions evaluated for slurry optimization.

Experiment Number	Conditions	Response variable
1	E1 – 400 μm 5%PVDF – 5%SuperP – 90% LNMO or LFP	Discharge Capacity (mAh g^{-1})
2	E2 – 350 μm 7.5%PVDF – 5%SuperP87.5% LNMO or LFP	Discharge Capacity (mAh g^{-1})
3	E2 – 450 μm 7.5%PVDF – 5%SuperP87.5% LNMO or LFP	Discharge Capacity (mAh g^{-1})
4	E3 – 400 μm 7.5%PVDF –7.5%SuperP85% LNMO or LFP	Discharge Capacity (mAh g^{-1})
5	E4 – 350 μm 7.5%PVDF – 10%SuperP82.5% LNMO or LFP	Discharge Capacity (mAh g^{-1})
6	E4 – 450 μm 7.5%PVDF – 10%SuperP82.5% LNMO or LFP	Discharge Capacity (mAh g^{-1})
7	E5 – 400 μm 10%PVDF – 5%SuperP85% LNMO or LFP	Discharge Capacity (mAh g^{-1})
8	E6 – 350 μm 5%PVDF – 7.5%SuperP87.5% LNMO or LFP	Discharge Capacity (mAh g^{-1})
9	E6 – 450 μm 5%PVDF – 7.5%SuperP87.5% LNMO or LFP	Discharge Capacity (mAh g^{-1})
10	E7 – 400 μm 5%PVDF – 10%SuperP85% LNMO or LFP	Discharge Capacity (mAh g^{-1})
11	E8 – 350 μm 10%PVDF – 7.5%SuperP82.5% LNMO or LFP	Discharge Capacity (mAh g^{-1})
12	E8 – 450 μm 10%PVDF – 7.5%SuperP82.5% LNMO or LFP	Discharge Capacity (mAh g^{-1})
13	E9 – 400 μm 10%PVDF – 10%SuperP80% LNMO or LFP	Discharge Capacity (mAh g^{-1})

Appendix B. Supplementary data

Supplementary data to this article can be found online at https://doi.org/10.1016/j.seta.2026.104997.

Data availability

Data will be made available on request.

References

[1] Wang N, Yin J, Li H, Wang T, Cui S, Yan W, et al. Recent advance in Mn-based Li-rich cathode materials: Oxygen release mechanism and its solution strategies based on electronic structure perspective, spanning from commercial liquid batteries to all-solid-state batteries. Next Mater 2025;6:100408. https://doi.org/10.1016/J.NXMATE.2024.100408.

[2] Han D, Park K, Park JH, Yun DJ, Son YH. Selective doping of Li-rich layered oxide cathode materials for high-stability rechargeable Li-ion batteries. J Ind Eng Chem 2018;68. https://doi.org/10.1016/j.jiec.2018.07.044.

[3] Lu C, Yang S, Wu H, Zhang Y, Yang X, Liang T. Enhanced electrochemical performance of Li-rich Li1.2Mn0.52Co0.08Ni0.2O2 cathode materials for Li-ion batteries by vanadium doping. Electrochim Acta 2016;209:448–55. https://doi.org/10.1016/J.ELECTACTA.2016.05.119.

[4] Yu H, Zhou H. High-energy cathode materials (Li2MnO3–LiMO2) for lithium-ion batteries. J Phys Chem Lett 2013;4:1268–80. https://doi.org/10.1021/JZ400032V.

[5] Shodiev A, Chouchane M, Gaberscek M, Arcelus O, Xu J, Oularbi H, et al. Deconvoluting the benefits of porosity distribution in layered electrodes on the electrochemical performance of Li-ion batteries. Energy Storage Mater 2022;47. https://doi.org/10.1016/j.ensm.2022.01.058.

[6] Zhu P, Slater PR, Kendrick E. Insights into architecture, design and manufacture of electrodes for lithium-ion batteries. Mater Des 2022;223. https://doi.org/10.1016/j.matdes.2022.111208.

[7] Liu T, Liu J, Li L, Yu L, Diao J, Zhou T, et al. Origin of structural degradation in Li-rich layered oxide cathode. Nature 2022;606. https://doi.org/10.1038/s41586-022-04689-y.

[8] Kim JK, Cheruvally G, Ahn JH, Hwang GC, Choi JB. Electrochemical properties of carbon-coated LiFePO4 synthesized by a modified mechanical activation process. J Phys Chem Solid 2008;69:2371–7. https://doi.org/10.1016/j.jpcs.2008.03.018.

[9] Yamada A, Koizumi H, Nishimura SI, Sonoyama N, Kanno R, Yonemura M, et al. Room-temperature miscibility gap in LixFePO4. Nat Mater 2006;5:357–60. https://doi.org/10.1038/nmat1634.

[10] Li Z, Peng Z, Zhang H, Hu T, Hu M, Zhu K, et al. [100]-Oriented LiFePO 4 Nanoflakes toward High Rate Li-Ion Battery Cathode. Nano Lett 2016;16:795–9. https://doi.org/10.1021/acs.nanolett.5b04855.

[11] Wang L, He X, Sun W, Wang J, Li Y, Fan S. Crystal Orientation Tuning of LiFePO 4 Nanoplates for High Rate Lithium Battery Cathode Materials. Nano Lett 2012;12:5632–6. https://doi.org/10.1021/nl3027839.

[12] Chen G, An J, Meng Y, Yuan C, Matthews B, Dou F, et al. Cation and anion Co-doping synergy to improve structural stability of Li- and Mn-rich layered cathode materials for lithium-ion batteries. Nano Energy 2019;57. https://doi.org/10.1016/j.nanoen.2018.12.049.

[13] Kwon NH, Conder J, Srout M, Fromm KM. Surface modifications of positive-electrode materials for lithium ion batteries. Chimia (Aarau) 2019;73. https://doi.org/10.2533/chimia.2019.880.

[14] Meng H, Li L, Liu J, Han X, Zhang W, Liu X, et al. Surface modification of Li-rich layered Li[Li0.17Ni0.17Co0.10Mn0.56]O2oxide with LiV3O8as a cathode material for Li-ion batteries. J Alloy Compd 2017;690. https://doi.org/10.1016/j.jallcom.2016.08.089.

[15] Wang D, Xu T, Li Y, Pan D, Lu X, Hu YS, et al. Integrated Surface Functionalization of Li-Rich Cathode Materials for Li-Ion Batteries. ACS Appl Mater Interfaces 2018;10. https://doi.org/10.1021/acsami.8b16319.

[16] Salgado RM, Danzi F, Oliveira JE, El-Azab A, Camanho PP, Braga MH. The latest trends in electric vehicles batteries. Molecules 2021;26:1–41. https://doi.org/10.3390/molecules26113188.

[17] Danner T, Singh M, Hein S, Kaiser J, Hahn H, Latz A. Thick electrodes for Li-ion batteries: a model based analysis. J Power Sources 2016;334. https://doi.org/10.1016/j.jpowsour.2016.09.143.

[18] Song K, Zhang C, Hu N, Wu X, Zhang L. High performance thick cathodes enabled by gradient porosity. Electrochim Acta 2021;377. https://doi.org/10.1016/j.electacta.2021.138105.

[19] Zhang J, Qiao J, Sun K, Wang Z. Balancing particle properties for practical lithium-ion batteries. Particuology 2022;61. https://doi.org/10.1016/j.partic.2021.05.006.

[20] Li M, Zhou S, Cheng L, Ren W, Chen L, Yu S, et al. Vertical-channel hierarchically porous 3D printed electrodes with ultrahigh mass loading and areal energy density for Li-ion batteries. Energy Storage Mater 2024;72:103754. https://doi.org/10.1016/J.ENSM.2024.103754.

[21] Lu C, Wu W, Wang L, Tian R, Du F. Thick electrode for energy storage systems: a facile strategy towards high energy density Li ion batteries. Next Mater 2024;4:100170. https://doi.org/10.1016/J.NXMATE.2024.100170.

[22] Zhu P, Slater PR, Kendrick E. Insights into architecture, design and manufacture of electrodes for lithium-ion batteries. Mater Des 2022;223:111208. https://doi.org/10.1016/J.MATDES.2022.111208.

[23] Guo Y, Jiang Y, Zhang Q, Wan D, Huang C. Directional LiFePO4 cathode structure by freeze tape casting to improve lithium ion diffusion kinetics. J Power Sources 2021;506:230052. https://doi.org/10.1016/J.JPOWSOUR.2021.230052.

[24] Wang Z, Zhao Z, Yang Y, Zhang A, Liu X, Zhao T, et al. Clarification of the dispersion mechanism of cathode slurry of lithium-ion battery under effects of both poly vinylidene fluoride/carbon black ratio and mixing time. Particuology 2024;88:116–27. https://doi.org/10.1016/J.PARTIC.2023.08.020.

[25] Mori T, Ochi T, Kitamura K. Characterization of slurries for lithium-ion battery cathodes by measuring their flow and change in hydrostatic pressure over time and clarification of the relationship between slurry and cathode properties. J Colloid Interface Sci 2023;629:36–45. https://doi.org/10.1016/J.JCIS.2022.08.192.

[26] Mun SC, Jeon YH, Won JH. Progress and challenges for replacing n-methyl-2-pyrrolidone / polyvinylidene fluoride slurry formulations in lithium-ion battery cathodes. Prog Nat Sci: Mater Int 2024;34:194–206. https://doi.org/10.1016/J.PNSC.2024.02.013.

[27] Ouyang L, Wu Z, Wang J, Qi X, Li Q, Wang J, et al. The effect of solid content on the rheological properties and microstructures of a Li-ion battery cathode slurry. RSC Adv 2020;10:19360–70. https://doi.org/10.1039/D0RA02651D.

[28] Agudelo HD, Vasquez FA, Calderón JA. Cobalt-Free Oxide Cathode Material with phase Composition Control to High Electrochemical Performance in Li-Ion Batteries. J Electrochem Soc 2024;171. https://doi.org/10.1149/1945-7111/ad1c15.

[29] Wang L, He X, Sun W, Wang J, Li Y, Fan S. Crystal orientation tuning of LiFePO4 nanoplates for high rate lithium battery cathode materials. Nano Lett 2012;12:5632–6. https://doi.org/10.1021/NL3027839/SUPPL_FILE/NL3027839_SI_001.PDF.

[30] Orozco-Gallo DC, Vásquez-Arroyave FA, Calderón-Gutierréz JA. Carbon-slurry optimization for lithium-ion batteries customization. Electrochim Acta 2023;467:143141. https://doi.org/10.1016/j.electacta.2023.143141.

[31] Markevich E, Sharabi R, Haik O, Borgel V, Salitra G, Aurbach D, et al. Raman spectroscopy of carbon-coated LiCoPO4 and LiFePO 4 olivines. J Power Sources 2011;196. https://doi.org/10.1016/j.jpowsour.2011.03.059.
[32] Dong YZ, Zhao YM, Duan H. Crystal structure and lithium electrochemical extraction properties of olivine type LiFePO4. Mater Chem Phys 2011;129:756–60. https://doi.org/10.1016/j.matchemphys.2011.04.076.
[33] Huang X, He X, Jiang C, Tian G. Morphology evolution and impurity analysis of LiFePO4 nanoparticles via a solvothermal synthesis process. RSC Adv 2014;4: 56074–83. https://doi.org/10.1039/c4ra09484k.
[34] Hu G, Qi X, Hu K, Lai X, Zhang X, Du K, et al. A facile cathode design with a LiNi0.6Co0.2Mn0.2O2 core and an AlF3-activated Li1.2Ni0.2Mn0.6O2 shell for Li-ion batteries. Electrochim Acta 2018;265:391–9. https://doi.org/10.1016/j.electacta.2018.01.176.
[35] Dai S, Liu Z, Zhao B, Zeng J, Hu H, Zhang Q, et al. A high-performance supercapacitor electrode based on N-doped porous graphene. J Power Sources 2018;387:43–8. https://doi.org/10.1016/J.JPOWSOUR.2018.03.055.
[36] Lu J, Chen Z, Pan F, Cui Y, Amine K. High-performance anode materials for rechargeable lithium-ion batteries. Electrochem Energy Rev 2018;1:35–53. https://doi.org/10.1007/S41918-018-0001-4/FIGURES/8.
[37] Goodenough JB, Park KS. The Li-ion rechargeable battery: a perspective. J Am Chem Soc 2013;135:1167–76. https://doi.org/10.1021/JA3091438/ASSET/IMAGES/MEDIUM/JA-2012-091438_0009.GIF.
[38] Malik R, Burch D, Bazant M, Ceder G. Particle size dependence of the ionic diffusivity. Nano Lett 2010;10:4123–7. https://doi.org/10.1021/NL1023595/SUPPL_FILE/NL1023595_SI_001.PDF.
[39] AbdelHamid AA, Mendoza-Garcia A, Ying JY. Advances in and prospects of nanomaterials' morphological control for lithium rechargeable batteries. Nano Energy 2022;93:106860. https://doi.org/10.1016/J.NANOEN.2021.106860.
[40] Ye N, Yan T, Jiang Z, Wu W, Fang T. A review: conventional and supercritical hydro/solvothermal synthesis of ultrafine particles as cathode in lithium battery. Ceram Int 2018;44:4521–37. https://doi.org/10.1016/J.CERAMINT.2017.12.236.
[41] Konda K, Jacob MS, Seth JR, Juvekar VA, Gopalan R, Moodakare SB. Capacity degradation of lithium-ion cell: the role of free carbon black content in the slurry and drying induced cracks in LiFePO4 electrode. J Energy Storage 2023;74: 109477. https://doi.org/10.1016/J.EST.2023.109477.
[42] Mayer JK, Bockholt H, Kwade A. Inner carbon black porosity as characteristic parameter for the microstructure of lithium-ion electrodes and its effect on physical and electrochemical properties. J Power Sources 2022;529:231259. https://doi.org/10.1016/J.JPOWSOUR.2022.231259.
[43] Kwon NH, Conder J, Srout M, Fromm KM. Surface modifications of positive-electrode materials for lithium ion batteries. Chimia (Aarau) 2019;73:880. https://doi.org/10.2533/chimia.2019.880.
[44] Yang P, Li H, Wei X, Zhang S, Xing Y. Structure tuned Li1.2Mn0.6Ni0.2O2 with low cation mixing and Ni segregation as high performance cathode materials for Li-ion batteries. Electrochim Acta 2018;271:276–83. https://doi.org/10.1016/J.ELECTACTA.2018.01.104.
[45] Cai W, Yan C, Yao Y-X, Xu L, Xu R, Jiang L-L, et al. Rapid lithium diffusion in order@disorder pathways for fast-charging graphite anodes. Small Struct 2020;1: 2000010. https://doi.org/10.1002/sstr.202000010.
[46] Gervillié-Mouravieff C, Albero Blanquer L, Alphen C, Huang J, Tarascon JM. Unraveling SEI formation and cycling behavior of commercial Ni-rich NMC Li-ion pouch cells through operando optical characterization. J Power Sources 2023;580: 233268. https://doi.org/10.1016/j.jpowsour.2023.233268.
[47] Qiu Y, Geng Y, Yu J, Zuo X. High-capacity cathode for lithium-ion battery from LiFePO4/(C + Fe2P) composite nanofibers by electrospinning. J Mater Sci 2014; 49. https://doi.org/10.1007/s10853-013-7727-5.
[48] Xie Y, Jin Y, Xiang L. Li-rich layered oxides: Structure, capacity and voltage fading mechanisms and solving strategies. Particuology 2022;61. https://doi.org/10.1016/j.partic.2021.05.011.
[49] Tu W, Wen Y, Ye C, Xing L, Xu K, Li W. Phase transformation of lithium-rich oxide cathode in full cell and its suppression by solid electrolyte interphase on graphite anode. Energy Environ Mater 2020;3. https://doi.org/10.1002/eem2.12034.
[50] Sangsanit T, Matkhaw N, Benwannamas N, Songthan R, Tejangkura W, Sawangphruk M. Layered lithium- and manganese-rich oxide cathode cells in large-scale cylindrical configuration: Optimized electrolyte formulations with LiDFOB and $LiBF_4$ Co-additives for enhanced stability. J Power Sources 2025;632:236337. https://doi.org/10.1016/J.JPOWSOUR.2025.236337.